PERGAMON

International Journal of Multiphase Flow 29 (2003) 1–21

International Journal of Multiphase Flow

www.elsevier.com/locate/ijmulflow

Concentration of pulp fibers in 3D turbulent channel flow

S. Dong, X. Feng, M. Salcudean *, I. Gartshore

Department of Mechanical Engineering, University of British Columbia, Vancouver, Canada V6T 1Z4

Received 16 March 2002; received in revised form 7 October 2002

Abstract

The concentration of pulp fibers in three-dimensional fully developed turbulent channel flow is investigated by two numerical methods: a random-walk simulation and large eddy simulation (LES). For the random-walk simulation, the Reynolds averaged Navier–Stokes equations are solved for the mean flow fields with Reynolds number 65,000 (based on average channel velocity and channel half-width). The individual components of the fluctuation velocities are obtained by curve-fitting existing experimental data for the whole channel width. The LES is performed at Reynolds number Re_τ (based on friction velocity and channel half-width) of 2820, which is close to the flow condition used for the random-walk simulation. A flexible fiber model is used to simulate the fiber motion. A general wall model is developed to deal with the fiber interaction with the walls. Both simulated results show that the concentration increases linearly near the wall and becomes approximately constant farther from the wall, in reasonable agreement with experimental observations.

Keywords: Fiber concentration; Turbulence; Random walk; Large eddy simulation

1. Introduction

Two-phase turbulent dispersed flow has many engineering applications. The focus of the present work is the fiber-dispersed turbulent flow that occurs in a pulp and paper device such as a screen. Screening is an important process in both chemical and mechanical pulping (Kumar, 1991; Olson, 1996; Gooding, 1986, 1996; Gooding et al., 2001). Understanding the fiber motion and fiber concentration in the flow approaching the screen plate is a key part of predicting the screen fractionation efficiency. The object of this paper is to study numerically the fiber concentration in

* Corresponding author.
E-mail address: msal@interchange.ubc.ca (M. Salcudean).

0301-9322/03/$ - see front matter
PII: S0301-9322(02)00128-3

3D turbulent channel flow which has similar flow conditions as that in the flow upstream of the screen.

In general, there are two approaches to predict two-phase flow. One is an Eulerian approach, in which the solid phase (particles) is regarded as a continuum and the governing equations are solved for both phases. The other is a Lagrangian approach, which treats the particles as distinct entities within the fluid phase. The random-walk simulation uses the Lagrangian frame to solve the particle trajectory equations as the particle interacts with a succession of discrete turbulent eddies. Randomly drawn turbulent fluctuations are used to determine the instantaneous velocity of the flow field. Kallio and Reeks (1989) used a random-walk model to calculate the particle concentration in two-dimensional turbulent flow using a linear Stokes drag and Saffman lift forces for small spheres. The velocity field was obtained from the log-law and the near wall velocity fluctuation velocities normal to the wall were obtained by assuming a Gaussian distribution with rms values that were curve-fitted from experimental results. Kroger and Drossinos (2000) followed this approach to simulate particle distributions in isothermal and heated turbulent boundary layers.

Both the Eulererian and Lagrangian approaches need good predictions of the turbulent flow. Three numerical methods can be used for modeling the turbulence: direct numerical simulation (DNS), Reynolds averaged Navier–Stokes (RANS) and large eddy simulation (LES). DNS provides a complete time dependent solution of the Navier–Stokes and continuity equations. DNS assumes that the size of the smallest eddies in any turbulent flow is of the order of the Kolmogorov microscale and specifies the grids so that these eddies can be resolved. Unfortunately, DNS can only be used for very small Reynolds number problems using current computer resources. Simulations of particles in wall bounded flows using DNS with low Reynolds number have been performed by McLaughlin (1989), Pedinotti et al. (1992), Brooke et al. (1992, 1994), Rouson and Eaton (1994), Chen et al. (1995) and Haarlem et al. (1998).

For RANS methods, the mean velocity and mean pressure are solutions of the RANS and continuity equations, the entire spectrum of velocity fluctuations are modeled by a single series of assumptions such as the well-known κ–ε model. RANS could be used to calculate the particle trajectory in turbulent flow when it is coupled with other tools to get the effect of the individual velocity fluctuation components.

The third method to simulate the flow field is LES. In LES, the large scales of motion are calculated directly from the Navier–Stokes equations while the small scales of motion are modeled. LES employs a mesh resolution coarser than that used by DNS but fine enough to resolve the large-scale eddies and uses a subgrid-scale (SGS) model only for those eddies whose size is smaller than the mesh spacing. LES is much more accurate than RANS and it can also be applied to relatively high Reynolds number problems. Wang and Squires (1996) used LES to investigate the particle transport in fully developed turbulent channel flow with Reynolds numbers, Re_τ, of 180 and 644.

From the literature, most of the particles studied in the particle-laden turbulent flow are assumed to be rigid, smooth spheres with a radius that is small compared to the Kolmogorov length scale of the flow. The density of the particles is usually larger than that of the fluid. The particles tend to accumulate near the wall. Brooke et al. (1994) claimed that the near wall concentration buildup comes from particles that arrive in free flight from distances far from the wall and are trapped in the viscous sublayer where normal velocity fluctuations of the fluid are very small.

There are only a few theoretical studies of highly elongated particles or fibers in turbulent flow. Kagermann and Köhler (1982) considered non-interacting rigid spheroids suspended in a homogeneous turbulent flow. A renormalized expansion is used to derive a kinetic equation whose coefficients are determined by the Lagrangian correlation function of the turbulent velocity field and by the translational diffusion coefficients and the orientational relaxation frequency of the spheroid. The assumption is made that the particle is smaller than the smallest scales of turbulence and the velocity field is statistically homogeneous, stationary and Gaussian with zero mean. Krushkal and Gallily (1988) calculated the orientation distribution function of small non-spherical aerosol particles using the Fokker–Planck equation.

Pulp fibers have high aspect ratios and can have considerable flexibility. Wherrett (1996) modeled a fiber as a series of bounded elements based on the work of Yamamoto and Matsuoka (1993, 1994) for 2D flow. The translation and rotation equations of each sphere determined the fiber motion. The results for a rigid fiber matched Jeffery's theory (1922). But the computation time was somewhat long, the model was two-dimensional and had no wall interaction model, all of which would limit the usefulness for real industrial applications. Olson (1996) developed a theoretical model of fiber passage and verified the predictions of this model experimentally. But his model was restricted to rigid fibers. Lawryshyn (1997) introduced a method to calculate the dynamic movement of a flexible fiber in a two-dimensional plane based on Euler–Bernoulli beam bending theory, i.e. small deflection beam theory. Stockie and Green (1998) simulated the motion of flexible pulp fibers using the immersed boundary method, which is able to capture the influence of the fiber on the fluid. But their work was restricted to two-dimensional simulations. In order to simulate industrial applications, a three-dimensional flexible fiber model is necessary, together with a corresponding wall model, since the influence of walls is central to the operation of some of the pulp and paper equipment. In order to account for these characteristics, we have employed a flexible fiber model proposed by Ross and Klingenberg (1997) and developed a corresponding general wall model. The assumption for the fiber model is that the flow is Stokes flow, which means the Reynolds number based on the relative velocity between the fiber and the fluid is less than one. But the fibers were modeled as linked spheroids to save computational time.

Several experimental measurements have been carried out of the fiber concentration in turbulent flow similar to that approaching a screen. Gooding (1986) and Gooding and Kerekes (1989) investigated the motion of 3 mm fibers at five heights near a wall and found that there are fewer fibers in the "exit layer" than in the mainstream flow. Olson (1996) experimentally determined the detailed distribution of fiber concentration for a range of fiber lengths. The channel velocity in the experiment is 7.1 m/s and the channel Reynolds number is about 71,000. Dyed nylon fibers of length 3.1, 2.0, 1.1 mm with diameter 40 microns were used. The fiber concentration was less than 5000 fibers/l so that the fiber–fiber interaction was negligible. The object of the present paper is to simulate numerically the fiber concentration in the turbulent flow near a solid wall by a random-walk model and LES methods, and to compare the results with Olson's (1996) experimental measurements.

We assume the fiber suspension is dilute and we ignore the fiber–fiber interaction and the effects of the fiber on the turbulent flow. If a particle of density ρ_p and radius a moves in a fluid of dynamic viscosity μ and friction velocity u_τ, the Stokes number (Crowe et al., 1985) was defined as $St = \tau_p/\tau_f$: the ratio of the particle response time $\tau_p = 2\rho_p a^2/9\mu$ and some fluid time scale

$\tau_f = H/2u_\tau$ (Rouson and Eaton, 1994, H is the channel width). If the stokes number is very small, than the particle just follows the flow; if it is very large, the particle will not be affected by turbulent fluctuations; if the Stokes number is in the order of one, the particle will be affected by the turbulence but cannot be the flow tracer (Fessler et al., 1994). In the current simulation, if we take a as the typical long radius of the spheroid, the response time is about 0.05 s and St is about 1.9. So the fiber is expected to be affected by the turbulence and it does not exactly follow the flow.

Section 2 describes the flow simulation methods that were used. Sections 3 and 4 describe the fiber and near wall fiber models respectively. Section 5 gives a description of the numerical algorithms and validation of the fiber motion. The numerical results from the random walk and LES are presented in Section 6. A brief summary in Section 7 concludes the paper.

2. Flow calculation

This section displays the two turbulent flow calculation methods and solvers used in the paper. The first method is the random-walk method (Section 2.1) and the second is the LES method (Section 2.2).

The height of the channel is 0.02 m (z direction) in both random-walk and LES calculations, which is the about the same as that of Olson (1996). In the random-walk calculation, the length of the channel is 0.4 m (x direction) and the spanwise size (y direction) is 0.01 m. In the LES calculation, the length of the channel is 0.048 m and the spanwise size is 0.02857 m.

2.1. Random-walk method

In the random-walk method, the turbulent flow velocity is decomposed into mean and fluctuating parts.

2.1.1. Mean velocity

The mean velocities are given by numerical solutions of the RANS and continuity equations, which are given by (i stands for 1, 2, 3 direction):

$$\frac{\partial U_i}{\partial x_i} = 0, \tag{1}$$

$$\frac{\partial U_i}{\partial t} + U_j \frac{\partial U_i}{\partial x_j} = -\frac{1}{\rho}\frac{\partial P}{\partial x_i} + \frac{1}{\rho}\frac{\partial}{\partial x_j}\left(\mu \frac{\partial U_i}{\partial x_j} + \tau_{ij}\right), \tag{2}$$

where U_i is the mean velocity vector, P is the mean pressure and μ is the molecular viscosity of the fluid. $\tau_{ij} = -\rho\overline{u_i' u_j'}$ is known as the Reynolds-stress tensor, which introduces 6 unknown quantities as a result of Reynolds averaging. $i = 1, 2, 3$ refers to the x (streamwise), y (spanwise) and z (normal) directions, respectively. The usual summation notation applies here. The Reynolds-stress

tensor needs a model or another equation for closure, and often takes the form of a Boussinesq approximation:

$$\tau_{ij} = 2\mu_T S_{ij} - \tfrac{2}{3}\rho\kappa\delta_{ij}, \tag{3}$$

where μ_T is eddy viscosity, S_{ij} is the mean strain-rate tensor which is given by

$$S_{ij} = \frac{1}{2}\left(\frac{\partial U_i}{\partial x_j} + \frac{\partial U_j}{\partial x_i}\right) \tag{4}$$

and $\kappa = \frac{1}{2}\overline{u_i' u_i'}$ is the turbulence kinetic energy. To close the system (1) and (2), we used the standard κ–ε model as follows. The assumptions for this model are that the effective viscosity must be isotropic and that the Reynolds number must be high enough to produce a fully turbulent flow.

Eddy viscosity

$$\mu_T = \rho C_\mu \kappa^2/\varepsilon. \tag{5}$$

Turbulence kinetic energy

$$\rho\frac{\partial \kappa}{\partial t} + \rho U_j \frac{\partial \kappa}{\partial x_j} = \tau_{ij}\frac{\partial U_i}{\partial x_j} - \rho\varepsilon + \frac{\partial}{\partial x_j}\left[(\mu + \mu_T/\sigma_\kappa)\frac{\partial \kappa}{\partial x_j}\right]. \tag{6}$$

Dissipation rate

$$\rho\frac{\partial \varepsilon}{\partial t} + \rho U_j \frac{\partial \varepsilon}{\partial x_j} = C_1\frac{\varepsilon}{\kappa}\tau_{ij}\frac{\partial U_i}{\partial x_j} - C_2\rho\frac{\varepsilon^2}{\kappa} + \frac{\partial}{\partial x_j}\left[(\mu + \mu_T/\sigma_\varepsilon)\frac{\partial \varepsilon}{\partial x_j}\right]. \tag{7}$$

Closure coefficients are given their standard values:

$$C_1 = 1.44, \quad C_2 = 1.92, \quad C_\mu = 0.09, \quad \sigma_\kappa = 1.0, \quad \sigma_\varepsilon = 1.3. \tag{8}$$

The κ–ε turbulent model is not valid in the near wall region where the influence of laminar viscosity is important. The RANS solver uses the wall-function treatment described by Launder and Spalding (1974), assuming different velocity profiles (log-law when $y^+ \geqslant 11.36$, linear when $y^+ < 11.36$) in the near wall region.

A finite volume method in conjunction with general curvilinear grids and domain segmentation method is used in the solver. The physical tangential velocity components are used as the dependent variables for the momentum equation and discretization is done by directly using the coordinate-invariant governing equations. A uniform velocity boundary condition is applied at the inlet, a gradient boundary condition is applied at the outlet, and a wall condition is used on the top and bottom channel walls. Symmetry boundary conditions are used in the spanwise direction.

2.1.2. Fluctuation velocity

Gosman and Ioannides (1981), Shuen et al. (1983, 1985) and Adeniji-Fashola et al. (1988) assumed that the turbulence is isotropic and calculated the fluctuations by a Gaussian distribution whose variance is given by

$$\sigma^2 = \tfrac{2}{3}\kappa, \tag{9}$$

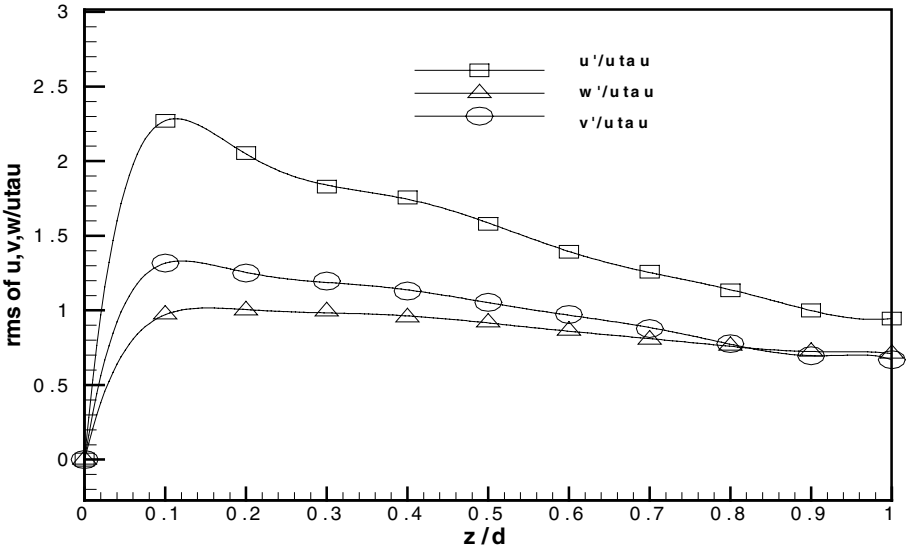

Fig. 1. Rms velocity by 8th order curve-fitting Comte-Bellot's experiment data.

where κ is the turbulent kinetic energy of the flow. Because the turbulence field in the channel is anisotropic near the wall, Eq. (9) may not be accurate enough. Instead, we use the variances measured by Comte-Bellot's experiment (1965) for fully developed turbulent channel flow with $Re_\tau = 2340$, which is close to the condition simulated here. Unfortunately, there is no data in the region where the channel height z is less than 0.1 times of the half channel height. In order to fill this gap, we add one point $(0,0)$ at the origin and use 8th order polynomials to curve-fit the resulting experimental data (Fig. 1).

The vorticity fluctuations are also required for the motion of the fibers. We examined two different approximations: Type I assumes that the vorticity is given by the formulae:

$$\omega'_x = 0.5\left(\frac{\partial v'}{\partial z} - \frac{\partial w'}{\partial y}\right), \quad \omega'_y = 0.5\left(\frac{\partial w'}{\partial x} - \frac{\partial u'}{\partial z}\right), \quad \omega'_z = 0.5\left(\frac{\partial u'}{\partial y} - \frac{\partial v'}{\partial x}\right),$$

where u', v', w' are the total velocities including the mean velocities and the fluctuation velocities. Type II assumes that the vorticity fluctuation components are randomly drawn from a Gaussian probability density of zero mean and $\varepsilon/0.09\kappa$ standard deviation. Wilcox (1988) presented $\varepsilon/0.09\kappa$ for his κ–ε model and identified it as "the RMS fluctuating vorticity" (Wilcox and Alber, 1972). These two types of approximation give the similar results. The instantaneous velocity and angular velocity are assumed to influence the fiber motion during a given time period, the residence time, before a new fluctuation component is sampled. The residence time of the fiber in the present eddy is determined by $T = \min(T_1, L/V)$, where T_1 is turbulence time scale κ/ε, L is the approximate size of a local eddy $C_\mu^{3/4}\kappa^{3/2}/\varepsilon$, and $V = \sqrt{u_r^2 + v_r^2 + w_r^2}$, where (u_r, v_r, w_r) is the relative velocity of the fiber with respect to the fluid. The fiber will stay in the same eddy until T expires. Because anisotropic flow has three unique time scales, the current technique is only for simplicity and may not apply to the real turbulence flow.

2.2. Large eddy simulation (LES)

The equations governing the transport of the large eddies, obtained by filtering the Navier–Stokes equations, are

$$\frac{\partial \bar{u}_i}{\partial x_i} = 0, \tag{10}$$

$$\frac{\partial \bar{u}_i}{\partial t} + \bar{u}_j \frac{\partial \bar{u}_i}{\partial x_j} = -\frac{1}{\rho}\frac{\partial \bar{p}}{\partial x_i} + \frac{1}{\rho}\frac{\partial}{\partial x_j}\left(\mu \frac{\partial \bar{u}_i}{\partial x_j} - \tau_{ij}\right), \tag{11}$$

where $\bar{u}_i$ is the filtered velocity, $\bar{p}$ is the filtered pressure, τ_{ij} is the SGS stress tensor. Eqs. (10) and (11) have similar forms to the RANS equations (1) and (2).

We used the first SGS stress model proposed by Smagorinsky (1963). His model assumes that the SGS stress follows a gradient-diffusion process, similar to molecular motion. Consequently, τ_{ij} is given by the eddy viscosity assumption

$$\tau_{ij} - \tfrac{1}{3}\delta_{ij}\tau_{kk} = -2\nu_T \bar{S}_{ij}, \tag{12}$$

where

$$\nu_T = (C_s f_s \Delta_s)^2 |\bar{S}|, \quad |\bar{S}| = \sqrt{2\bar{S}_{ij}\bar{S}_{ij}}, \quad \bar{S}_{ij} = \frac{1}{2}\left(\frac{\partial \bar{u}_i}{\partial x_j} + \frac{\partial \bar{u}_j}{\partial x_i}\right)$$

is the filtered rate of strain tensor and C_s is the Smagorinsky constant ($0.1 \leqslant C_s \leqslant 0.24$, Rogallo and Moin, 1984). Here $\Delta_s = (\Delta x_1 * \Delta x_2 * \Delta x_3)^{1/3}$ is filter width, Δx_i ($i = 1, 2, 3$) is i direction mesh size. $f_s = 1 - \exp(-y^+/25)$ is the damping function needed in the vicinity of the wall. In the current calculation, we set $C_s = 0.1$.

The governing equations are discretized on a staggered grid using the finite volume method in curvilinear coordinates. The staggered grids avoid oscillations in the computed pressure. A fractional step method (Ferziger and Peric, 1996; Kim and Moin, 1985) is employed. The pressure gradient and the incompressibility constraint are integrated implicitly in time. The space derivative is approximated by the second-order central scheme. The convective and diffusive terms are treated explicitly by a two-stage Adams-Bashforth scheme. The Poisson-like pressure equation is solved to satisfy the mass continuity. The fast Fourier transform is applied in the direction of periodicity, and the cyclic reduction method is then used to solve the 2D Poisson equation. Parallel computing is used for the LES. The domain is decomposed in one direction and the data is distributed into multiprocessors. The communication occurs only at block boundaries. Message Passing Interface is used to exchange the data among the processors. The parallel solver runs well on PIII/Linux cluster (University of British Columbia) and MACI Compaq Alpha Cluster (University of Calgary).

One hundred non-uniform grids are used in z (wall) direction and the first grid near the wall is about 0.013 mm. The uniform grid size in the x direction is 0.6 mm and in the y direction is 0.57 mm. For the height below 1 mm, the turbulence length scale based on $\kappa^{1.5}/\varepsilon$ is between 0.09 and 1.9 mm. The grid size 0.5 and 0.75 mm in x direction have also been tested and the results for 0.5 mm grid is very close to the results of 0.6 mm. Fig. 2 includes the mean velocity and the

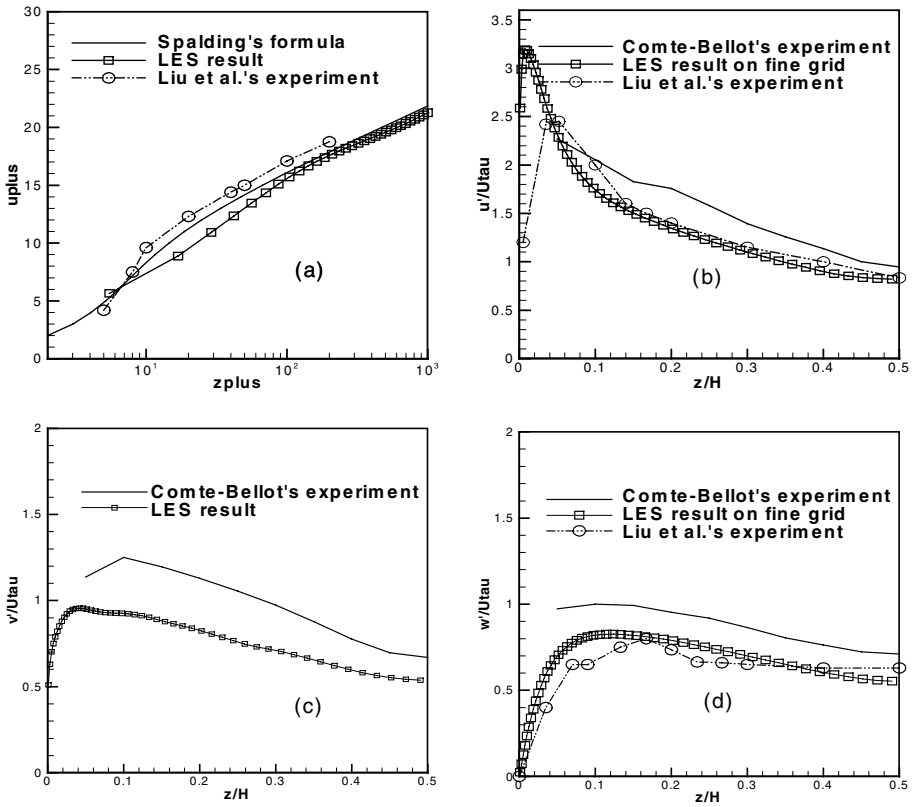

Fig. 2. Mean and fluctuation velocities calculated by LES: (a) mean velocity with Spalding's formula and Liu et al.'s experiment; (b) u'/u_τ with Comte-Bellot's experiment ($Re_\tau = 2340$) and Liu et al.'s experiment ($Re_\tau = 184$); (c) v'/u_τ with Comte-Bellot's experiment ($Re_\tau = 2340$) (Liu et al.'s experiment not available); (d) w'/u_τ with Comte-Bellot's experiment ($Re_\tau = 2340$) and Liu et al.'s experiment ($Re_\tau = 184$).

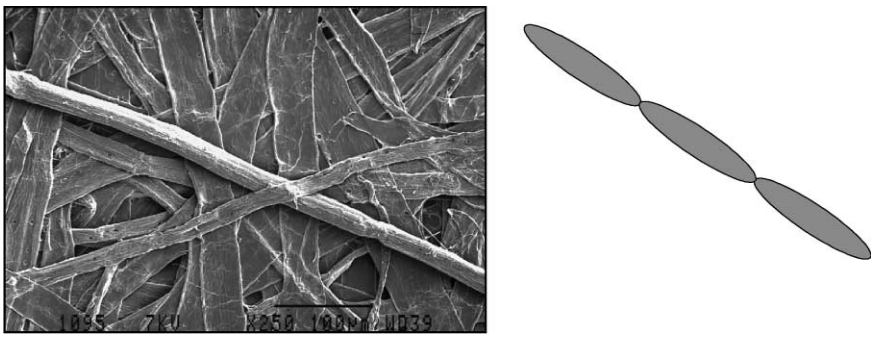

Fig. 3. A photo of a rigid fiber (provided by Olson) and a plot of the model of a fiber.

fluctuation velocities calculated by LES. The mean velocity is compared with Liu et al.'s experiment (1991) and Spalding's single composite formula (1961) that covered the entire wall region with $k = 0.41$, $B = 5.0$:

$$z^+ = u^+ + \mathrm{e}^{-\kappa B}\left[\mathrm{e}^{\kappa u^+} - 1 - \kappa u^+ - \frac{(\kappa u^+)^2}{2} - \frac{(\kappa u^+)^3}{6}\right].$$

The fluctuation velocities are compared with Comte-Bellot's experimental data (1965) and Liu et al.'s experiment (1991). We see that there are some differences between the simulated fluctuations and the experimental data. The Reynolds numbers for the experiments and the simulations are not the same, and the LES data includes only the contributions from the largest eddy motions.

3. Fiber model

Each fiber is modeled as a chain of spheroids linked together by joints. Fig. 3 is a photo and a plot of a fiber modeled. Both rigid and flexible fibers can be modeled by changing the bending constant of the joints. The motion of the fiber is determined by solving each spheroid's translation and rotation equations that are derived based on Newton's second law and the law of moment of momentum. The model is based on the assumption that the fluid inertia is negligible and that the hydrodynamic force has a linear relation with the difference between the fluid velocity and the fiber velocity.

The hydrodynamic force and torque on the spheroid i are obtained from Kim and Karrila (1991) (i for spheroid and j for direction):

$$\begin{aligned}
\vec{F}_i^{(\mathrm{h})} &= 6\pi\mu a[X^A d_i d_j + Y^A(\delta_{ij} - d_i d_j)] \cdot (\vec{U}_j^{(\infty)} - \overrightarrow{V_j}),\\
\vec{M}_i^{(\mathrm{h})} &= 8\pi\mu a^3[X^A d_i d_j + Y^A(\delta_{ij} - d_i d_j)] \cdot (\vec{\Omega}_j^{(\infty)} - \vec{\omega}_j) - 8\pi\mu a^3 Y^H \varepsilon_{ijk} d_i d_k \vec{E}_{jk}^{(\infty)},
\end{aligned} \tag{13}$$

where $U_j^{(\infty)}$ is fluid velocity. The fluid velocities at the center of each spheroid are obtained by trilinear interpolating the velocities at the corners of the cell where the center of the spheroid lies. $E^{(\infty)}$ and $\Omega^{(\infty)}$ are the rate of strain tensor and vorticity respectively, the general forms of these quantities become:

$$\begin{aligned}
&E_{11} = \frac{\partial u}{\partial x}, \quad E_{22} = \frac{\partial v}{\partial y}, \quad E_{33} = \frac{\partial w}{\partial z}, \quad E_{12} = \frac{1}{2}\left(\frac{\partial u}{\partial y} + \frac{\partial v}{\partial x}\right),\\
&E_{13} = \frac{1}{2}\left(\frac{\partial u}{\partial z} + \frac{\partial w}{\partial x}\right), \quad E_{23} = \frac{1}{2}\left(\frac{\partial v}{\partial z} + \frac{\partial w}{\partial y}\right),\\
&\Omega_1 = \frac{1}{2}\left(\frac{\partial v}{\partial z} - \frac{\partial w}{\partial y}\right), \quad \Omega_2 = \frac{1}{2}\left(\frac{\partial w}{\partial x} - \frac{\partial u}{\partial z}\right), \quad \Omega_3 = \frac{1}{2}\left(\frac{\partial u}{\partial y} - \frac{\partial v}{\partial x}\right),
\end{aligned} \tag{14}$$

where μ is the dynamic viscosity, and d_i is the unit directional vector along the axis. δ_{ij} is the Kronecker delta, which is the component of the identity tensor δ and equals one or zero according to i equal j or not. In addition, ε_{ijk} is the component of the alternating tensor ε defined by the relationship $\vec{a} \times \vec{b} = \varepsilon_{ijk} a_j b_k$ being valid for arbitrary vectors $\vec{a}$ and $\vec{b}$.

X^A, Y^A, X^C, Y^C, Y^H are resistance functions, which are dependent on the prolate spheroid eccentricity $e = \sqrt{(a^2 - b^2)}/a$, where a, b ($b \leqslant a$) are the major and minor axes lengths of the prolate spheroid. Near-spheres ($e \leqslant 1$) and needles ($e \to 1$) are two asymptotic cases of prolate spheroids and for these the resistance functions are in Table 1. Because the density difference between the

Table 1
Coefficients for the force and torque for the fiber

Resistance functions	Prolate spheroids ($0 < e < 1$)	Near-spheres ($e \leqslant 1$)	Needles ($e \to 1$) $\varepsilon = \sqrt{1-e^2} \leqslant 1$, $E = (\ln(2/\varepsilon))^{-1}$
X^A	$\frac{8}{3}e^3[-2e+(1+e^2)L]^{-1}$	$1-\frac{2e^2}{5}-\frac{17e^4}{175}+\cdots$	$\frac{4E}{6-3E}-\frac{(8-6E)E\varepsilon^2}{12-12E+3E^2}+\cdots$
Y^A	$\frac{16}{3}e^3[2e+(3e^2-1)L]^{-1}$	$1-\frac{3e^2}{10}-\frac{57e^4}{700}+\cdots$	$\frac{8E}{6+3E}-\frac{4E^2\varepsilon^2}{12+12E+3E^2}+\cdots$
X^C	$\frac{4}{3}e^3(1-e^2)[2e-(1-e^2)L]^{-1}$	$1-\frac{6e^2}{5}+\frac{27e^4}{175}+\cdots$	$\frac{2\varepsilon^2}{3}+\frac{(2-2E)E^4}{3E}+\cdots$
Y^C	$\frac{4}{3}e^3(2-e^2)[-2e+(1+e^2)L]^{-1}$	$1-\frac{9e^2}{10}+\frac{18e^4}{175}+\cdots$	$\frac{2E}{6-3E}+\frac{E^2\varepsilon^2}{12-12E+3E^2}+\cdots$
Y^H	$\frac{4}{3}e^5[-2e+(1+e^2)L]^{-1}$	$\frac{e^2}{2}-\frac{e^4}{5}+\cdots$	$\frac{2E}{6-3E}-\frac{(8-5E)E\varepsilon^2}{12-12E+3E^2}+\cdots$

fiber and the water is very small, the mass force is neglected. Currently, there is no lift force added to the model.

The resulting rotation equation is

$$\sum_{l=1}^{N} Q_{il}\cdot\vec{\omega}_l = D_i, \tag{15}$$

where

$$\begin{aligned} Q_{il} &= \delta_{il}C_i^{(\mathrm{h})} - \sum_{j=1}^{N}\tilde{d}_{ij}\cdot A_j^{(\mathrm{h})}\cdot\tilde{b}_{lj} + \sum_{j=1}^{N}\sum_{k=1}^{N}\tilde{d}_{ij}\cdot A_j^{(\mathrm{h})}\cdot(A)^{-1}A_k^{(\mathrm{h})}\cdot\tilde{b}_{lk},\\ \vec{D}_i &= \vec{M}_i^{(\mathrm{w})} - \sum_{j=1}^{N}\vec{d}_{ij}\times\left[A_j^{(\mathrm{h})}\cdot\vec{U}_j^{(\infty)} + \vec{F}_j^{(g)} + \overrightarrow{FT}_j^{(\mathrm{w})} - A_j^{(\mathrm{h})}\cdot(A)^{-1}\right.\\ &\quad\left.\cdot\sum_{k=1}^{N}\left(A_k^{(\mathrm{h})}\cdot\vec{U}_k^{(\infty)} + \vec{F}_k^{(g)} + \overrightarrow{FT}_k^{(\mathrm{w})}\right)\right] + 8\pi\mu a^3\left[X^C d_i d_j + Y^C(\delta_{ij}-d_i d_j)\right]\cdot\vec{\Omega}_j^{(\infty)}\\ &\quad - 8\pi\mu a^3 Y^H\varepsilon_{ijk}d_l d_k\vec{E}_{jk}^{(\infty)} + \sum_{j=1}^{N}S_{ij}\vec{Y}_j, \end{aligned} \tag{16}$$

and

$$\tilde{d}_{ij} = \begin{bmatrix} 0 & -dz_{ij} & dy_{ij}\\ dz_{ij} & 0 & -dx_{ij}\\ -dy_{ij} & dx_{ij} & 0 \end{bmatrix},\quad \tilde{b}_{ij} = \begin{bmatrix} 0 & -bz_{ij} & by_{ij}\\ bz_{ij} & 0 & -bx_{ij}\\ -by_{ij} & bx_{ij} & 0. \end{bmatrix}. \tag{17}$$

The translation equation of motion for each spheroid is

$$\vec{V}_i = \sum_{j=1}^{N}\vec{\omega}_j\times\vec{b}_{ji} - (A)^{-1}\cdot\left[\sum_{j=1}^{N}\sum_{k=1}^{N}A_j^{(\mathrm{h})}\cdot(\vec{\omega}_k\times\vec{b}_{kj}) - \sum_{j=1}^{N}\left(A_j^{(\mathrm{h})}\cdot\vec{U}_j^{(\infty)} + \vec{F}_j^{(g)} + \overrightarrow{FT}_j^{(\mathrm{w})}\right)\right]. \tag{18}$$

$F_i^{(g)} = (4/3)\pi ab^2\Delta\rho g$ is body force that is ignored in the current calculation, because the density difference between the fiber and the water $\Delta\rho$ is small. $FT_j^{(\mathrm{w})}$ is the force due to the wall. $M_i^{(\mathrm{w})}$ is the

torque, which $FT_j^{(w)}$ generates. If the fiber does not touch the wall, both $FT_j^{(w)}$ and $M_i^{(w)}$ are zero. If the fiber touches the wall, they will be calculated and the details of calculation are shown in Section 4. Y_i is the resulting internal torque. The bending torque is $Y_i^{(B)} = k_B(\theta_i - \theta_i^{(0)})\mathbf{n}$, where k_B is a bending constant that takes the form of EI/a, where E is Young's modulus and I is the moment of inertia. Both rigid and flexible fibers can be modeled by changing this constant. θ_i is the angle between the adjacent spheroids, $\theta_i^{(0)}$ is its equilibrium angle, $\mathbf{n}$ is the unit vector normal to the plane of bending. $\overrightarrow{d_{ij}} = -(\vec{C}T)_{ij}$, $\overrightarrow{b_{ij}} = -(\vec{C}Tv)_{ij}$, where $\vec{C}$ is $N \times N$ matrix with components $C_{ij} = S_{ij}\overrightarrow{c_{ij}}$, with $v_{ij} = \delta_{ij} - 1/N$, $\overrightarrow{c_{ij}}$ as body-fixed connectivity vectors, extending from the center of the mass of the spheroid i to joint j. For a joint j not connected with spheroid i, this vector is defined as $\vec{0}$.

Connectivity matrices S and T are defined as:

$$S = \begin{bmatrix} -1 & 1 & 0 & \cdots & 0 \\ 0 & -1 & 1 & \ddots & \vdots \\ & & \ddots & \ddots & 0 \\ \vdots & & \ddots & -1 & 1 \\ 0 & & \cdots & 0 & -1 \end{bmatrix}, \quad T = \begin{bmatrix} -1 & -1 & -1 & \cdots & -1 \\ 0 & -1 & -1 & \cdots & -1 \\ & & -1 & \cdots & -1 \\ \vdots & & \ddots & \ddots & \vdots \\ 0 & & \cdots & 0 & -1 \end{bmatrix}. \tag{19}$$

4. Wall model

Fibers frequently touch the wall in pulp and paper equipment, so a wall model that could efficiently deal with the fiber–wall interaction needs to be developed. For the smooth slot geometry, Olson (1996) developed a two-dimensional wall model based on the assumption that a reaction force is exerted on the fiber to stop it passing through the solid wall and the friction force is proportional to the normal force on the fiber. Lawryshyn (1997) used a similar approach. Because the pulp and paper equipment has many different shapes of wall geometry, a three-dimensional universal wall model is developed, which could deal with the fiber interaction with any wall geometry. Section 4.1 introduces the question of judging whether a fiber touches the wall. Section 4.2 gives the equations of the fiber when it touches the wall.

4.1. The condition for the fiber to touch the wall

The wall surface is composed of grid cells. If the grid used for the flow calculation is coarse, it can be refined into smaller equal intervals in any direction. Fig. 4 is a schematic diagram showing the fiber touching the wall. If the fiber touches the wall, the system of the single spheroid and the refined grid line segment has a solution. The equation of the refined grid line segment is

$$\begin{cases} x = x_0 + \alpha(x_1 - x_0), \\ y = y_0 + \alpha(y_1 - y_0), \\ z = z_0 + \alpha(z_1 - z_0) \end{cases} \quad 0 \leqslant \alpha \leqslant 1, \tag{20}$$

where (x_0, y_0, z_0), (x_1, y_1, z_1) is the position of the two vertex of the line segment. The equation of the spheroid in fiber coordinates is

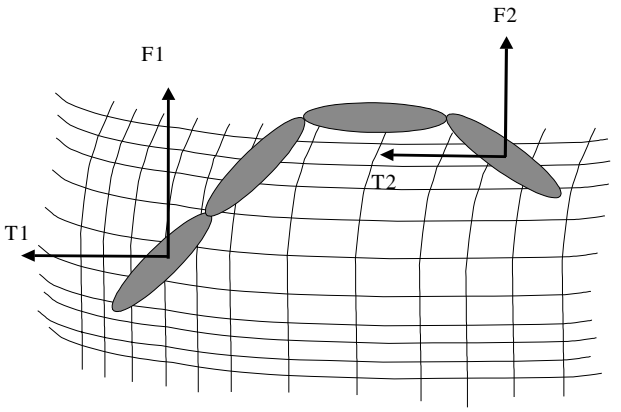

Fig. 4. Schematic diagram of the fiber touching the wall.

$$\frac{x_f^2}{a^2}+\frac{y_f^2}{b^2}+\frac{z_f^2}{b^2}=1. \tag{21}$$

If the transformation matrix that transforms the fixed coordinates to the fiber coordinates is TR, and (x_c, y_c, z_c) is the fiber center in the world coordinates, then the position in the fiber coordinate is

$$\begin{pmatrix} x_f \\ y_f \\ z_f \end{pmatrix} = \begin{pmatrix} \mathrm{tr}(1,1) & \mathrm{tr}(1,2) & \mathrm{tr}(1,3) \\ \mathrm{tr}(2,1) & \mathrm{tr}(2,2) & \mathrm{tr}(2,3) \\ \mathrm{tr}(3,1) & \mathrm{tr}(3,2) & \mathrm{tr}(3,3) \end{pmatrix} \begin{pmatrix} x-x_c \\ y-y_c \\ z-z_c \end{pmatrix}. \tag{22}$$

The spheroid equation then becomes

$$\begin{aligned} &\frac{[\mathrm{tr}(1,1)(x-x_c)+\mathrm{tr}(1,2)(y-y_c)+\mathrm{tr}(1,3)(z-z_c)]^2}{a^2} \\ &+\frac{[\mathrm{tr}(2,1)(x-x_c)+\mathrm{tr}(2,2)(y-y_c)+\mathrm{tr}(2,3)(z-z_c)]^2}{b^2} \\ &+\frac{[\mathrm{tr}(3,1)(x-x_c)+\mathrm{tr}(3,2)(y-y_c)+\mathrm{tr}(3,3)(z-z_c)]^2}{b^2}=1. \end{aligned} \tag{23}$$

If the system of (20) and (23) has a solution, then we say the fiber touches the wall.

4.2. The equation of the spheroid if it touches the wall

When the fiber touches the wall, the assumption for the forces added to the spheroid is that the normal force is always perpendicular to the wall, and the tangential friction force is proportional to the normal force. If ith-spheroid touches the wall, then the normal force for this spheroid is

$$\overrightarrow{F_i}=\overrightarrow{fc_i}\cdot f_i=\begin{pmatrix} fx \\ fy \\ fz \end{pmatrix}_i \cdot f_i,$$

where

$$\overrightarrow{fc}_i = \begin{pmatrix} fx \\ fy \\ fz \end{pmatrix}_i$$

is the unit normal vector generated from the normal of the contacted wall surface and f_i is the magnitude of the normal force. The unit tangential vector

$$\begin{pmatrix} tx \\ ty \\ tz \end{pmatrix}_i$$

is:

$$\begin{pmatrix} tx \\ ty \\ tz \end{pmatrix}_i = -\begin{pmatrix} tu \\ tv \\ tw \end{pmatrix}_i \Big/ \mathrm{vel}_i, \tag{24}$$

where

$$\begin{pmatrix} tu \\ tv \\ tw \end{pmatrix}_i = \begin{pmatrix} u \\ v \\ w \end{pmatrix}_i - \mathrm{unor}_i \cdot \begin{pmatrix} fx \\ fy \\ fz \end{pmatrix}_i,$$

$$\mathrm{vel} = (tu^2 + tv^2 + tw^2)^{0.5}, \tag{25}$$

$$\mathrm{unor}_i = \begin{pmatrix} u \\ v \\ w \end{pmatrix}_i \bullet \begin{pmatrix} fx \\ fy \\ fz \end{pmatrix}_i$$

and $(u, v, w)_i$ are the ith-spheroid velocities.

The coefficient of the total force added to the ith-spheroid is

$$\begin{pmatrix} ftx \\ fty \\ ftz \end{pmatrix}_i = \begin{pmatrix} fx \\ fy \\ fz \end{pmatrix} + \eta \cdot \begin{pmatrix} tx \\ ty \\ tz \end{pmatrix}_i, \tag{26}$$

η is the coefficient of wall friction that is (somewhat arbitrarily) taken as 0.2 in all the simulations. Tests carried out have shown that the results were not sensitive to the choice of the friction coefficient. The added total force is

$$\overrightarrow{FT_i} = \begin{pmatrix} ftx \\ fty \\ ftz \end{pmatrix} \cdot f_i. \tag{27}$$

f_i needs to be calculated. Putting (27) into (15) and (18), the new velocities are found to consist of two parts:

$$\vec{V}_i = \overrightarrow{V_{\mathrm{old}\,i}} + \overrightarrow{V_{\mathrm{wall}\,i}}, \tag{28}$$

where $\overrightarrow{V_{\text{old}}}$ is exactly the form of (18) without wall contact. $\overrightarrow{V_{\text{wall}}}$ comes from the fiber–wall contact, which takes the form of

$$\overrightarrow{V_{\text{wall}i}} = \sum_{j=1}^{N} \overrightarrow{\omega_{\text{wall}j}} \times \vec{b}_{ji} - (A)^{-1} \cdot \left[\sum_{j=1}^{N} \sum_{k=1}^{N} A_j^{(\text{h})} \cdot (\overrightarrow{\omega_{\text{wall}k}} \times \vec{b}_{kj}) - \sum_{j=1}^{N} (\overrightarrow{FT}_j^{(\text{w})}) \right]. \tag{29}$$

$\overrightarrow{\omega_{\text{wall}j}}$ is obtained from the similar form of (15) with the same Q_{il} and different $\overrightarrow{D_i}$:

$$\vec{D}_i = -\sum_{j=1}^{N} \vec{d}_{ij} \times \left[\overrightarrow{FT}_j^{(\text{w})} - A_j^{(\text{h})} \cdot (A)^{-1} \cdot \sum_{k=1}^{N} (\overrightarrow{FT}_k^{(\text{w})}) \right]. \tag{30}$$

After using (27), (28) can also be written as

$$\vec{V}_i = \overrightarrow{V_{\text{old}\,i}} + \overrightarrow{VV}_i \cdot f_i, \tag{31}$$

where $\overrightarrow{VV_i}$ is (29) taking off f_i. Taking the product of (31) and the unit normal vector

$$\overrightarrow{fc}_i = \begin{pmatrix} fx \\ fy \\ fz \end{pmatrix}_i,$$

we get:

$$\overrightarrow{fc}_i \bullet \vec{V}_i = \overrightarrow{fc}_i \bullet \overrightarrow{V_{\text{old}\,i}} + \overrightarrow{fc}_i \bullet \overrightarrow{VV}_i \cdot f_i. \tag{32}$$

The LHS of (32) must be zero from the assumption that the fiber cannot go through the wall. $\overrightarrow{fc}_i \bullet \overrightarrow{V_{\text{old}\,i}}$ and $\overrightarrow{fc}_i \bullet \overrightarrow{VV}_i$ could be calculated from the above analysis. If $i = 1$ (only one spheroid touches the wall), (32) becomes a single equation with the unknown f_1; If $i \geqslant 2$ (more than one spheroid touch the wall), (32) becomes a system of equations with the unknowns f_i, $i \geqslant 2$.

After f_i is solved, the torque of spheroid j due to the wall force $F\vec{T}_j^{(\text{w})}$ is $\vec{M}_i^{(\text{w})} = (\vec{r}_j - \vec{r}_i) \times F\vec{T}_j^{(\text{w})}$ where $\vec{r}_j$ is the distance from the center of spheroid j to the origin. Eqs. (16) and (18) are solved when the fiber touches the wall.

5. Algorithms for the fiber motion and validation

The translation equation (18) is a first-order ordinary differential equation in spite of its complicated form. The general form of the first-order ordinary differential equation is:

$$\begin{cases} y' = f(t, y), \\ y(0) = \eta. \end{cases} \tag{33}$$

A first-order Euler method and a Variable Order Runge–Kutta Method are used for discretizing (33).

The Euler method is simple and easy to implement, but it is only a first-order scheme and the time step is also fixed. For the fiber motion in general pulp and paper equipment, a more accurate solution is needed. The computation time is also expected to be reduced for a large number of fiber calculations. Higher order methods are needed.

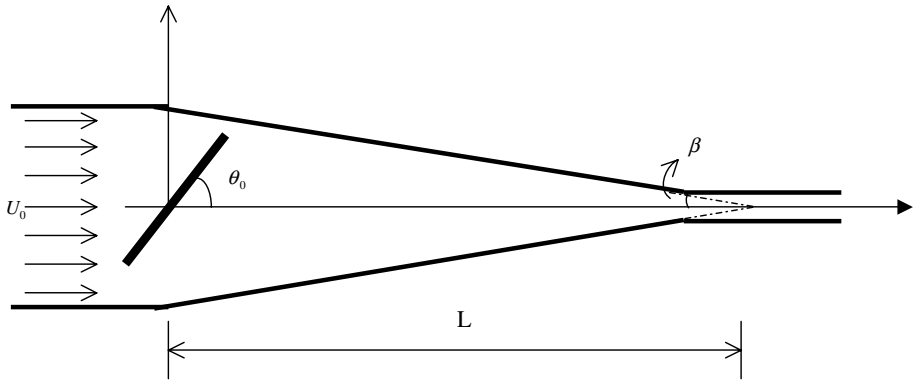

Fig. 5. Geometry of the symmetrical convergent section of a headbox.

Fibers frequently touch the wall in the practical equipment. Certain derivatives of the solution are very large in the near wall region or the region where the flow has rapid changes. In those regions, higher order solutions may have poor accuracy and lower order solutions may have very good accuracy. It is therefore necessary to use variable order methods for different regions. The variable order Runge–Kutta method is a family of explicit Runge–Kutta formulas. Each member of the family consists of a fifth-order formula that includes imbedded formulas of orders from 1 to 4. A proper order formula is chosen by calculating the solution at several different orders before the full Runge–Kutta step is computed. The detailed algorithm is included in the work of Cash and Karp (1990).

Jeffery (1922) first analyzed the motion of non-spherical particle. He derived the equations of the motion of an ellipsoid in a Newtonian flow. Kim and Karrila (1991) showed that as the spheroid rotates in the linear field, its axis traces a periodic trajectory which is same as Jeffery's orbit. In a simple shear flow, Skjetne et al. (1997) verified the single fiber trajectory calculated by the current fiber model with Jeffery's analysis. Dong (2002) has validated the fiber model and the variable order Runge–Kutta method using a more general example. The flow field of the symmetric convergent section of the headbox (Fig. 5) is approximated by

$$\begin{aligned} U(x) &= \frac{U_0}{1-\frac{x}{L}}, \\ V(x) &= -\frac{U_0}{L(1-\frac{x}{l})^2}y. \end{aligned} \tag{34}$$

By assuming that the center of the fiber moves along the centerline, the analytical alignment of the fiber is determined by Olson (1996):

$$\theta(x) = \arctan\left(\frac{\sin(2\theta_0)}{\cos(2\theta_0)+1}\left(1-2\frac{x}{L}+\left(\frac{x}{L}\right)^2\right)^{(\alpha_2-1)/(\alpha^2+1)}\right), \tag{35}$$

where $\theta = \theta_0$ at $t = 0$, and α is the aspect ratio of the fiber which is greater than or equal to one.

In the example, the contraction angle $\beta = 16.7°$, the inlet channel height is 150 mm and the outlet channel height is 15 mm. So the contraction length is $L = 250$ mm. Taking the initial

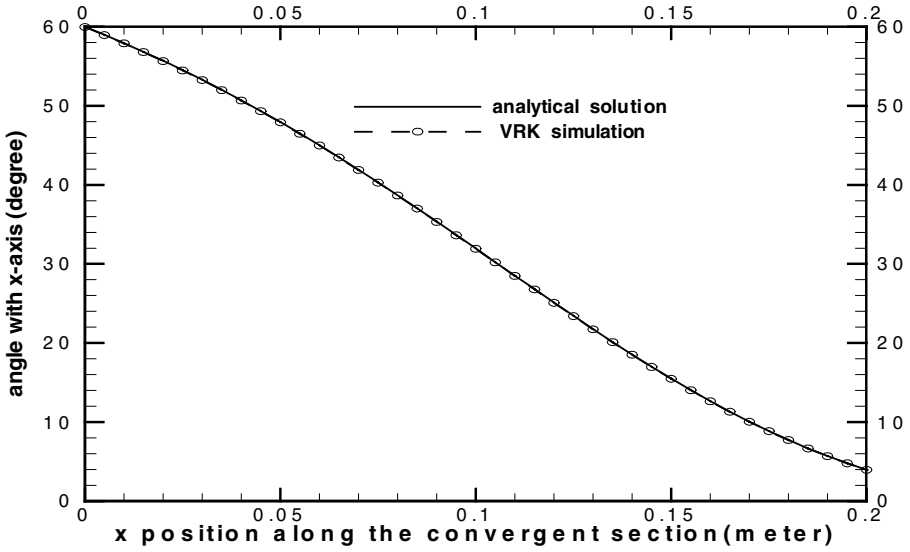

Fig. 6. Comparison of analytical solution and VRK solution.

alignment to be $\theta_0 = 60°$, Fig. 6 shows a comparison of the analytical solution with the simulation angle.

6. Numerical results

In order to record the fiber positions, several stations are set along the channel length. The channel height is divided into equal height intervals. The concentration ratio C/C_{av} is calculated by the ratio of the number of fibers at each height interval at each station to the average number of the fibers across the channel height. 8000 rigid fibers of 1, 2, 3 mm are initially chosen across the channel with random height and random orientation such that the number of fibers is about the same at each height interval. For a fixed length and diameter fiber, the number of the spheroids employed in the fiber can be relatively small to reduce the computation time, which is one of the benefits to model to fibers as linked spheroids. The results for using different number of spheroids are slightly different due to the treatment of the wall, but the global results remain unaffected. For the current simulation, 2–4 spheroids are used for 1 mm fiber simulation and 3–6 spheroids are used for 2–3 mm fiber simulation.

6.1. Results from random walk

For the random-walk calculation, non-uniform grids are used for the wall direction and uniform grids are used in the other two directions. The fibers are injected into the flow field after the flow field is converged by RANS. The flow field and the fiber motion are calculated separately. Fig. 7 presents the comparison of concentrations for different fiber lengths. Except for the area very near to the wall, the concentration increases, has a peak at a distance of about one-half fiber

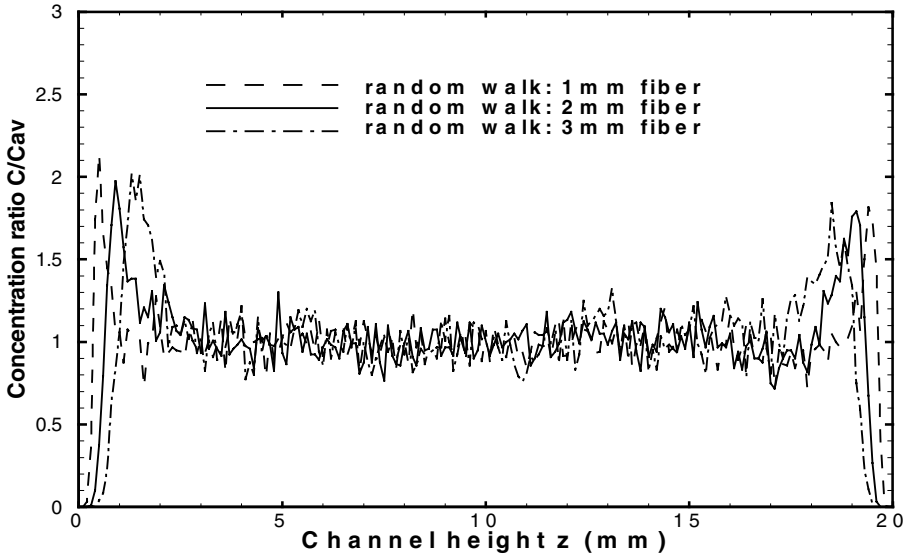

Fig. 7. Concentration for 1, 2 and 3 mm fibers vs. channel height, using random walk.

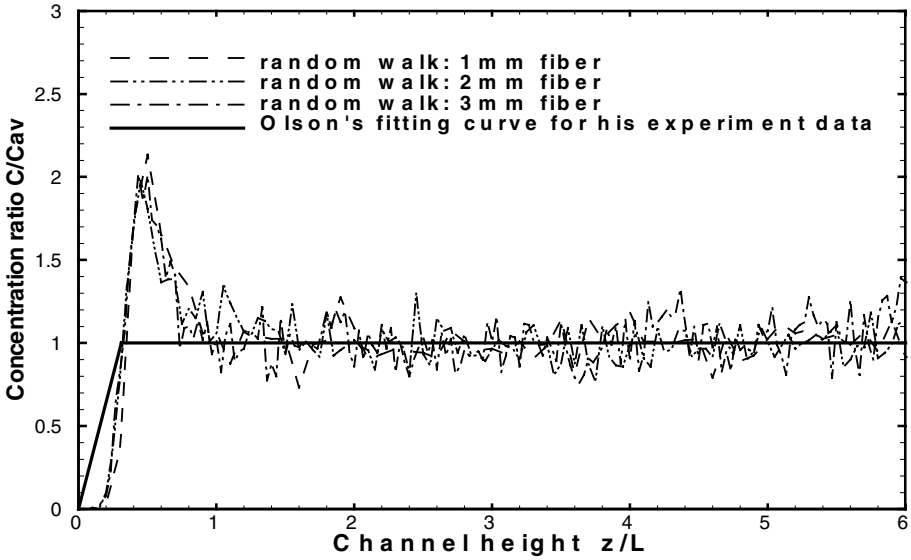

Fig. 8. Concentration for 1, 2 and 3 mm fibers vs. channel height scaled by fiber length, using random walk.

length and then tends to be 1. The slope for different fiber length is different. The smaller the fiber length, the steeper the slope. If the height is scaled by fiber length, the slopes collapse. (Fig. 8). This agrees reasonably well with Olson's fitted curve for his experiment (1996). Olson's fitted concentration curve is

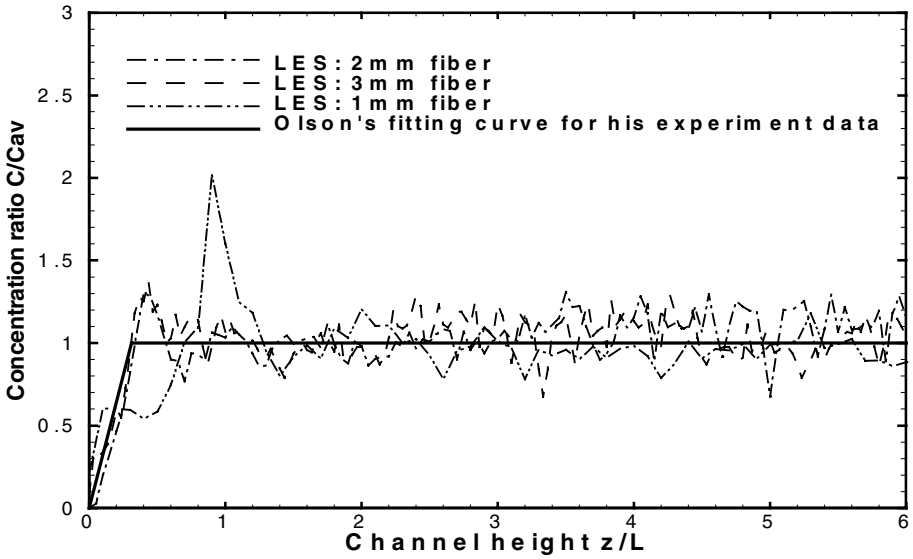

Fig. 9. Concentration for 1, 2 and 3 mm fiber vs. channel height scaled by fiber length using LES.

$$C/C_{\mathrm{av}} = \begin{cases} 3.22y/L, & y/L < 1/3.22, \\ 1, & y/L \geqslant 1/3.22. \end{cases} \tag{36}$$

6.2. Results from LES

After the flow field from LES is statistically steady, the fibers are put in. Then each LES time step calculation is followed by one step of the fiber motion. Fig. 9 shows the comparison of concentration for 1, 2, 3 mm fibers. We see that the concentration curve of 2 and 3 mm fibers are very close to the Olson's fitted curve. The 1 mm fiber does not have the same curve. The grid in x direction (0.6 mm) is probably too coarse for 1 mm fiber simulation.

For random-walk calculation, the flow field was calculated using the standard κ–ε model for isotropic flow, which is not exact for the near wall region. There is no experimental data for the velocity fluctuations very close to the wall. This limits the application of the random walk for fiber motion in the channel and other equipment. LES will constitute a better technique to simulate the fiber interaction in the future, particularly as better and faster computer resources are developed.

7. Summary and conclusion

A complete numerical tool to simulate fiber motion in turbulent flow has been developed. The flow distribution was computed first, in one of two different ways: either the RANS equations were solved with the κ–ε model of turbulence or a LES was used. The distribution of fiber concentration was then obtained using the computed flow in two corresponding ways: a random-walk method was developed to use the κ–ε predictions, and a direct calculation of fiber motion was

made, based on the detailed flow field computed by the LES method. The random-walk method uses experimental RMS distributions for the three components of velocity close to the wall, as these components are not predicted separately by the κ–ε turbulence model. In both cases a three-dimensional fiber model has been coupled to the flow to predict the fiber motion and a detailed wall model has been developed to deal with the fiber–wall interaction.

The two coupled models have been applied to predict the concentration of fibers in a fully developed three-dimensional channel flow (with channel height 20 mm, and average Reynolds number of 65,000 based on average channel velocity and channel half height). Particle trajectories and statistics have been obtained.

From the random-walk method, with fibers of 1, 2, 3 mm lengths, the concentration results scaled by the fiber length show a linear region near the wall and an almost constant region above a height of about half fiber length. Similar results were observed in the experiments of Olson (1996). A peak between the linear and constant concentration regions is observed in the simulation, a feature which also appears (with somewhat reduced magnitude) in Olson's (1996) data.

Using the LES method with different length fibers, the concentration curves of the 2 and 3 mm fibers are similar to the experiments. The 1 mm fiber results do not fit well with other computed or measured results, probably because the grid size for the LES calculation in the x direction (0.6 mm) is too coarse to model the turbulence adequately at the scale of the smallest fibers. A finer grid could not be used for the current LES calculation because of computer memory limitations.

The method for the simulation of fiber motion developed here can be used to model the behavior of fibers in other complex turbulent flows. The concentration simulation is the first step to predict the fiber passage in the screen. The fiber passage in several industrial screen slots was examined in Dong et al. (2000) and Dong (2002). This method has also been used to model the fiber separation in hydrocyclone (Wang, 2002; Wang et al., 2002) and the fiber orientation at the exit of the paper machine headbox (Dong et al., 2002). The LES method is more general, as it does not rely on experimental data and gives a better representation of the turbulence characteristics, but it is computationally much more expensive.

Acknowledgements

The authors are grateful to Dr. James Olson for his useful discussion. This work was supported by Forest Research of British Columbia (FRBC) and Natural Sciences and Engineering Research Council (NSERC). Simulations were carried on the PIII/Linux cluster at the University of British Columbia and MACI Compaq Alpha Cluster at the University of Calgary.

References

Adeniji-Fashola, A.A., Chen, C.P., Schafer, C.F., 1988. Numerical predictions of two-phase gas-particle flows using Eulerian and Lagrangian schemes. NASA Technical Paper.

Brooke, J.W., Kontomaris, K., Hanratty, T.J., McLaughlin, J.B., 1992. Turbulent deposition and trapping of aerosols at a wall. Phys. Fluids A 4, 825–834.

Brooke, J.W., Hanratty, T.J., McLaughlin, J.B., 1994. Free-flight mixing and deposition of aerosols. Phys. Fluids 6, 3404–3415.

Cash, J.R., Karp, A.H., 1990. A variable order Runge–Kutta method for initial value problems with rapidly varying right-hand sides. ACM Trans. Math. Software 16, 201–222.

Chen, M., Kontomaris, K., McLaughlin, J.B., 1995. Dispersion, growth and deposition of coalescing aerosols in a direct numerical simulation of turbulent channel flow. Gas-Particle Flows, ASME-FED 228, 27.

Comte-Bellot, G., 1965. Ecoulement turbulent entre des sparois parallels. Publ. Sci. Tech. Minis. Air, NR.

Crowe, C.T., Gore, R.A., Troutt, T.R., 1985. Particle dispersion by coherent structures in free shear flows. Part. Sci. Technol. 3, 149.

Dong, S., 2002. Modeling of fiber motion in pulp and paper equipment. Ph.D. thesis, University of British Columbia.

Dong, S., Salcudean, M., Gartshore, I., 2000. Fiber motion in single and multiple screen slot. 2000 TAPPI Papermakers Conference and Trade Fair.

Dong, S., Feng, X., Salcudean, M., Gartshore, I., Shariati, M., 2002. Turbulence and fiber orientation in the converging section of a paper-machine headbox. The 4th ASME/JSME/KSME Symposium on Computational Techniques for Fluid/Thermal/Chemical Systems with Industrial Applications. Vancouver, Canada.

Ferziger, J., Peric, M., 1996. Computational Methods for Fluid Dynamics, second ed. Springer.

Fessler, J.R., Kulick, J.D., Eaton, J.K., 1994. Preferential concentration of heavy particles in a turbulent channel flow. Phys. Fluids 6, 3742–3749.

Gooding, R.W., 1986. The passage of fibres through slots in pulp screening. M.A. Sc. thesis, University of British Columbia.

Gooding, R.W., 1996. Flow resistance of screen plate apertures. Ph.D. thesis, University of British Columbia.

Gooding, R., Kerekes, R.J., 1989. The motion of fibres near a screen slot. J. Pulp Paper Sci. 15, 59–62.

Gooding, R.W., Kerekes, R.J., Salcudean, M., 2001. The flow resistance of slotted apertured in pulp screens. Sci. Papermaking 1, 287–338.

Gosman, A.D., Ioannides, E., 1981. Aspects of computer simulation of liquid fueled combustors. AIAA paper, 81-0323.

Haarlem, B.V., Boersma, B.J., Nieuwstadt, F.T.M., 1998. Direct numerical simulation of particle deposition onto a free-slip and no-slip surface. Phys. Fluids 10, 2608–2620.

Jeffery, G.B., 1922. The motion of ellipsoidal particles immered in a viscous fluid. Proc. R. Soc. A 102, 161–179.

Kagermann, H., Köhler, W.E., 1982. On the motion of nonspherical particles in a turbulent flow. Physica 116A, 178–198.

Kallio, G.A., Reeks, M.W., 1989. A numerical simulation of particle deposition in turbulent boundary layers. Int. J. Multiphase Flow 15, 433–446.

Kim, J., Moin, P., 1985. Application of fractional-step method to incompressible Navier–Stokes equations. J. Comp. Phys. 59, 308–323.

Kim, S., Karrila, S.J., 1991. Microhydrodynamics: Principles and Selected Applications. Butterworth-Heinemann, Boston.

Kroger, C., Drossinos, Y., 2000. A random-walk simulation of thermophoretic particle deposition in a turbulent boundary layer. Int. J. Multiphase Flow 26, 1325–1350.

Krushkal, E.M., Gallily, I., 1988. On the orientation distribution function of non-spherical aerosol particles in a general shear flow—ii. The turbulent case. J. Aerosol Sci. 19, 197–211.

Kumar, A., 1991. Passage of fibers through screen apertures. Ph.D. thesis, University of British Columbia.

Launder, B.E., Spalding, D.B., 1974. The numerical computation of turbulent flows. Comput. Meth. Appl. Mech. Eng. 3, 269–289.

Lawryshyn, Y.A., 1997. Statics and dynamics of pulp fibers. Ph.D. thesis, University of Toronto.

Liu, Z.C., Landreth, C.C., Adrian, R.J., Hanratty, T.J., 1991. High resolution measurement of turbulent structure in a channel with particle image velocimetry. Exp. Fluids 10, 301–312.

McLaughlin, J.B., 1989. Aerosol particles deposition in numerically simulated channel flow. Phys. Fluid A 1, 1211.

Olson, J.S., 1996. The effect of fiber length on passage through narrow apertures. Ph.D. thesis, University of British Columbia.

Pedinotti, S., Mariotti, G., Banerjee, S., 1992. Direct numerical simulation of particle behaviour in the wall region of turbulent flows in horizontal channels. Int. J. Multiphase Flow 18, 927–941.

Rogallo, R.S., Moin, P., 1984. Numerical simulation of turbulent flows. Ann. Rev. Fluid Mech. 16, 99–137.

Ross, R.F., Klingenberg, D.J., 1997. Dynamic simulation of flexible fibers composed of linked rigid bodies. J. Chem. Phys. 106, 2949–2960.

Rouson, D.W.I., Eaton, J.K., 1994. Direct numerical simulation of turbulent channel flow with immersed particles. The 1994 ASME Fluids Engineering Division Summer Meeting, Lake Tahoe, NV.

Shuen, J.S., Solomon A.S.P., Zhang, Q.F., Faeth, G.M., 1983. A theoretical and experimental study of turbulent particle-laden jets. NASA CR 168293.

Shuen, J.S., Solomon, A.S.P., Zhang, Q.F., Faeth, G.M., 1985. Structure of particle-laden jets: measurements and predictions. AIAA J. 23, 396–404.

Skjetne, P., Ross, R.F., Klingenberg, D.J., 1997. Simulation of single fiber dynamics. J. Chem. Phys. 107, 2108–2121.

Smagorinsky, J., 1963. General circulation experiments with the primitive equations. Mon. Weather Rev. 91, 99–164.

Spalding, D.B., 1961. A single formula for the law of the wall. J. Appl. Mech. 28, 455–457.

Stockie, J.M., Green, S.I., 1998. Simulating the motion of flexible pulp fibers using the immersed boundary method. J. Comp. Phys. 147, 147–165.

Wang, Z., 2002. Numerical simulation of fiber separation in Hydrocyclones, M.A. Sc. thesis, University of British Columbia.

Wang, Q., Squires, K.D., 1996. Large eddy simulation of particle-laden turbulent channel flow. Phys. Fluids 8, 1207–1223.

Wang, Z., Dong, S., Saucudean, M., Gartshore, I., 2002. Fiber separation in hydrocyclones. 2002 TAPPI Fall Technical Conference and Trade Fair (Engineering and Pulping Conference), San Diego, CA.

Wherrett, G., 1996. Fiber motion in shear flow. M.A. Sc. thesis, University of British Columbia.

Wilcox, D.C., 1988. Reassessment of the scale determining equation for advanced turbulence models. AIAA J. 26, 1299–1310.

Wilcox, D.C., Alber, I.E., 1972. A turbulence model for high speed flows. In: Proc. of the 1972 Heat Trans. & Fluid Mech. Inst. Stanford Univ. Press, pp. 231–252.

Yamamoto, S., Matsuoka, T., 1993. A method for dynamic simulation of rigid and flexible fibers in a flow field. J. Chem. Phys. 98, 644–650.

Yamamoto, S., Matsuoka, T., 1994. Viscosity of dilute suspensions of rodlike particles: a numerical simulation method. J. Chem. Phys. 100, 3317–3324.